Investigation on the sensitivity of flexible foundation models of an offshore wind turbine under earthquake loadings

Yang Yang [a,b], Chun Li [a,*], Musa Bashir [b], Jin Wang [b], Chunmin Yang [c]

a. School of Energy and Power Engineering, University of Shanghai for Science and Technology, Shanghai, 200093, P.R. China

b. Department of Maritime and Mechanical Engineering, Liverpool John Moores University, Liverpool, Byrom Street, L3 3AF, UK

c. School of Electrical and Power Engineering, China University of Mining and Technology, Jiangsu 221116, P.R. China

Abstract: This paper presents an investigation on the sensitivity of flexible foundation models of offshore wind turbines subjected to earthquake loadings. A novel seismic analysis framework (SAF) is developed and implemented in an open source aero-hydro-elastic analysis tool, "FAST", for accurately modelling the effects of seismic loadings on offshore wind turbines. SAF has been validated through comparisons against experimentally validated numerical tools, GH Bladed and NREL Seismic. The behaviours of three flexible foundation models, namely, the apparent fixity (AF), coupled springs (CS) and distributed springs (DS) methods, subjected to earthquake loadings have been examined in relation to a fixed foundation. A total of 224 fully coupled nonlinear simulations of the foundation models are performed using a dataset of 28 earthquake records which are scaled using the target spectrum matching technique to represent the actual seismic effects of the selected sites. The results reveal that the AF model appropriately reflects realistic situations in comparison to the CS model. In addition, the amplitudes of vibration induced by the earthquake loadings are larger for

* Corresponding author: lichun_usst@163.com

flexible foundations compared to the rigid foundation. The main contribution to the out-of-plane bending moment of the support structure at the mudline comes from the wind loading for all the foundation models. This study has also found that the 2nd flap mode of blade is activated by the earthquake loadings for the AF and DS models but not for the rigid and CS models. As a result, the peak blade-root bending moment is found to be more sensitive to pseudo spectral acceleration (PSA) for the AF and DS models. Furthermore, the peak tower-top displacement and mudline bending moment increase linearly with PSA for all the examined models. This study contributes to the evaluation of the wind turbine responses subjected to earthquakes or combined multi-hazard loadings in the operational state.

Keywords: Offshore wind turbine; dynamic behaviour analysis; flexible foundation; earthquake loading.

1 Introduction

Wind energy is currently playing a leading role in the global production of cleaner energy as an alternative to fossil and non-cleaner fuels. The 2018 Global Wind Energy Council (GWEC) annual wind report states that 52 GW of newly installed wind capacity was added globally in 2017, and with 50 % of the figure shared by China and the USA [1]. The southeast coastal areas of China and the west coast of the USA, located close to the Pacific seismic belts, are prone to earthquake. Wind turbines installed in these areas are susceptible to damage from the resulting earthquake loading coupled with the local wind loading. Similar circumstances exist for the wind farms located along the southern areas of Europe and New Zealand where there are rich offshore wind resources. Therefore, it is imperative to investigate the impacts of earthquake loading on wind turbines due to potential consequences on operation and supply of wind energy in these locations.

Environmental loads acting on wind turbines along with earthquake loadings have a significant influence on the accuracy of the seismic analysis of wind turbines. Dynamic behaviours of wind turbines under earthquake excitations have been studied over the past decades but with simplifications on the model geometries [2-9]. In these studies, the rotor and nacelle were either completely ignored or simplified as a lumped mass. The unsteady wind loads are often treated as a rotor thrust, leading to inaccuracies in the prediction of aerodynamic loads acting on the blades. Generally, the aerodynamic loads increase exponentially with the rotor diameter for large-scale wind turbines. The resulting aerodynamic effects have been determined to be unneglectable from a comparative study on operational and parked states [10]. Therefore, over-simplification of aerodynamic loads is never precise, thereby undermining the accuracy of results in the seismic analysis of large-scale wind turbines. Therefore, in the seismic analysis of large-scale wind turbines, it is necessary to correctly take into account the coupled effect of wind and earthquake loadings.

One of the efficient approaches of improving the accuracy of coupled earthquake and wind loadings for wind turbines is by integrating an additional seismic module into an aeroelastic analysis tool. An early study on the coupled behaviour of earthquake and wind loadings was conducted by Witcher for a 2 MW wind turbine [11]. With the use of GH Bladed, Santangelo *et al.* [12] investigated the difference between the results from fully coupled and uncoupled time-domain simulations for a 5 MW wind turbine under the combined excitations of wind and earthquakes. Using FAST as a design basis, Asareh and Prowell [13-14] developed a seismic module in order to examine the coupled effect of wind and earthquake. In the seismic module, the calculation of the earthquake loading is based on a specific ground motion, and the stiffness and damping properties of a damped actuator are located at the tower-base. Asareh *et al.* [15] used the improved FAST (also called NREL Seismic) to investigate the relationships between earthquake intensity and structural responses. Jin *et al.* [16] also

used the NREL Seismic tool to predict the dynamic responses of a wind turbine under multiple hazards associated with earthquake and turbulent wind. Similarly, Yang *et al.* [8] proposed a numerical analysis framework coupled with FAST in order to obtain seismic responses of wind turbines. It is noted that the method of earthquake analysis proposed by Asareh and Prowell [13-14] is different from the one applied to seismic analysis of buildings. The accuracy of predictions is significantly influenced by the stiffness and damping properties. The selection of the values of stiffness and damping depends on the experience of the involved analytical engineers.

However, it is noted that most of the aforementioned literatures focused heavily on earthquake effects for land-based wind turbines, which are significantly different from the offshore types. Since a large number of newly installed offshore wind turbines are located in earthquake-prone areas, it is necessary to investigate the seismic behaviour of offshore wind turbines in order to mitigate potential consequences of damage caused by earthquakes.

Offshore wind turbines have slender support structures resulting in large vibration amplitudes at the tower-top. In addition, the nature of the soils in the offshore environment often leads to more severe structural responses. The offshore soil is composed of detrital materials and sediments, implying that the wind turbine foundation is installed in a layer of less dense and less stiff soil [18]. The soft soil condition is often associated with liquefaction in earthquake-prone offshore environments. This may affect the integrity or the serviceability of the foundation during its operational lifespan. As discussed by Wang *et al.* [19], the liquefaction is more easily caused by earthquakes leading to severe damage to the wind turbine under soft soil conditions. Some common foundation problems resulting from soil liquefaction include operational difficulty and loss of stability of the wind turbine. In addition, the cost of the foundation is approximately 30% of the total cost of a bottom-fixed offshore wind turbine and could reach up to 35% for the wind turbines installed

in water depth of 30 m ~ 40 m [20]. Hence, the deign of offshore wind turbine foundation subjected to earthquakes needs to be carefully handled due to its impact on the overall cost of wind turbines and the levelised cost of electricity (LCOE).

The soil structure interaction (SSI) model plays a key role in the design of a foundation as can be seen in Fig. 1. The accuracy of the results from foundation design analyses, including eigen-analysis and ultimate state analysis, is significantly influenced by the selection of the SSI model. This means that the selection of a SSI model determines the reliability of the foundation which costs over 30% of the whole wind turbine. Hence, the sensitivity analysis of SSI models is beneficial to the wind turbine industry for practical cost-reduction reasons when selecting the appropriate foundation concept during the design stage.

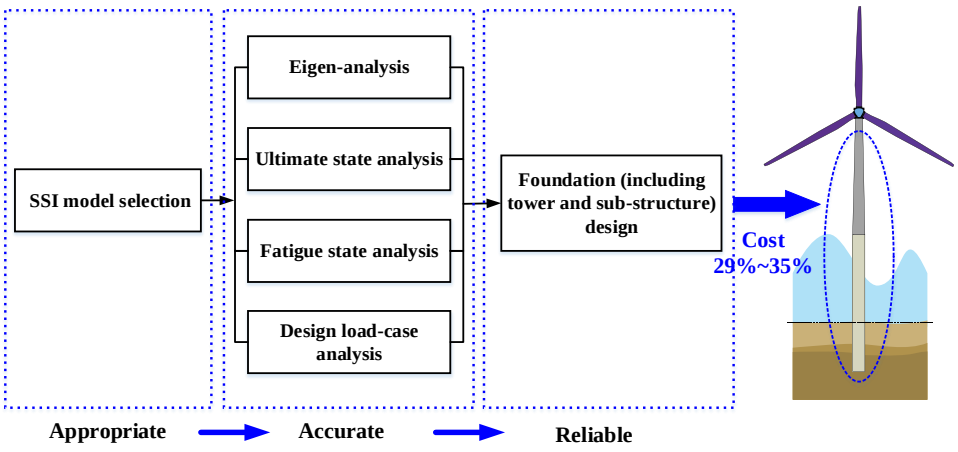

Fig. 1: The importance of SSI model to the foundation design for bottom-fixed offshore wind turbines

SSI can be modelled using three methods: apparent fixity (AF), coupled springs (CS) and distributed springs (DS) [21]. The CS model is the most widely used method in the dynamic analysis of offshore wind turbines and it is applicable to any type of offshore foundations due to its ease in obtaining results using typical theories [22-27]. For the CS model, the foundation is modelled using

a set of translational and rotational springs placed at the bottom of the structure to represent the SSI effect. Bhattacharya *et al.* [28-29] investigated the SSI of a monopile wind turbine under different soil conditions by using scaled experiments and numerical analysis. It was found that the numerical models had first natural frequencies similar to those of the test models in most soil conditions including clay. In some foundation cases with saturated sands, however, over 20% discrepancies were observed between the numerical and experimental results. In another study conducted by Bhattacharya *et al.* [30], it was found that the stiffness of lateral springs could be reduced under cyclic loadings, which is a major contributor to fatigue. The study found that 30% change in the first natural frequency of the wind turbine system occurred after 10,000 cycles. This suggests that there is a limitation on the use of the CS model for SSI modelling of the dense soil condition.

The DS model is another widely used foundation modelling method for SSI [31-36]. In this method, the SSI is represented by a set of lateral and vertical springs distributed along the embedded pile (usually, only the lateral springs are considered). The stiffness of the springs is obtained in accordance with *p-y* curves at different depths. Compared to the CS model, the DS model has an advantage that the responses of the embedded portion of the foundation can be investigated more specifically. The DS model is well suited for modelling pile in a multi-layered soil condition while the CS model could only model an overall effect of SSI at the seabed level.

The AF method is another modelling option which is an alternative to the CS and DS models. In this method, a fictive length is assumed to connect the bottom of the support structure and the foundation soils. The support structure is fixed and has the same mudline lateral deformation and rotation as the CS and DS models under external excitations. This approach is much easier to implement in any multi-body analysis tool for accounting the SSI effect. Damgaard *et al.* [37] investigated the dynamic responses of a monopile offshore wind turbine by considering the effect of

SSI modelled using AF and CS models. The AF model results in similar fatigue damage compared to the CS model for two distinct types of soil. From the preceding literatures, it has been noted that the SSI effect for offshore wind turbines has been examined under multiple loadings with the exception of earthquakes.

Santangelo *et al*. [38] compared the structural responses of coupled and uncoupled time-domain simulations for an offshore wind turbine under earthquake loadings. Kim *et al.* [39] investigated the seismic fragility of a monopile offshore wind turbine by considering the SSI effect. They modelled the flexible foundation using a set of lateral springs distributed along the length of the support structure underneath the seabed. The stiffness of each spring at a corresponding depth was represented by a *p-y* curve. Mo *et al*. [40] also performed a seismic fragility analysis of an offshore wind turbine under different operating states by considering the effect of SSI. Wind loads were calculated using FAST and then applied to the FEM model for coupling with earthquake loadings in OpenSees. The probability of reaching damage states was discussed for different wind conditions and earthquake loadings. Alati *et al.* [41] studied the seismic responses of two bottom-fixed offshore wind turbines using GH Bladed in which the SSI model was represented by two transitional springs.

However, there are still some notable limitations in the above-mentioned literatures. First, the dynamic characteristic in the frequency domain of offshore wind turbines under multi-loadings, which is important in the control and mitigation of vibration induced by an earthquake [42-43], has not been addressed. Secondly, although it has been widely accepted that the DS model offers the best approach for representing realistic foundation conditions, the difference between the three SSI modelling approaches (*i.e.* the AF, CS and DS) for seismic analysis of offshore wind turbines has not been thoroughly investigated. For offshore wind turbines located in earthquake-prone areas, the support structure suffers from high frequency and strong underlying excitations. This means that an

investigation of the sensitivity of flexible foundation models becomes imperative in order to perform accurate seismic analysis for a reliable foundation design.

The purpose of this study, therefore, is to investigate the sensitivity of foundation models of offshore wind turbines under multi-hazards by including earthquake, wind and wave loadings. The structural responses of the wind turbine with distinct foundation models will be examined in both time domain and frequency domain. For this purpose, a seismic analysis framework (SAF) is developed to take into account the influences of earthquake loading and foundation flexibility by extending the capability of the FAST source code. One of the benefits of using SAF is that it is generic and can be applied to different types of wind turbine models compared with the NREL Seismic tool presented in [14-15]. In addition, SAF offers capabilities for different SSI models to be examined as opposed to other tools that exclusively focus on the rigid foundation concept.

2 Seismic analysis framework modelling

In order to adequately examine the combined effects of earthquake, wind and wave in the design of offshore wind turbines, SAF for offshore wind turbines is developed and implemented in an open source numerical tool, FAST. The improved capability of the FAST-SAF means that comprehensive coupled analysis of wind turbine dynamics can be accurately performed by incorporating an appropriate foundation model. In this study, two subroutines (*UserTwrLd* and *UserPtfmLd*) in FAST have been extended to take into account the soil effect on flexible foundation models. This is additional to the *FAST.f90* source file being modified to implement the capability of seismic analysis. The seismic load calculated in SAF is coupled with the structural responses and other environmental loads in time domain. Detailed descriptions of FAST and SAF are presented in the subsequent sections.

2.1 FAST description

177 The FAST tool is used for accurate and efficient time domain simulations of wind turbines. The
178 baseline FAST which consists of four major modules (AeroDyn, HydroDyn, ServoDyn and ElastDyn)
179 is incapable of performing seismic analysis of fixed foundations in its current form [44]. In the
180 AeroDyn module, the dynamic wake model and blade element momentum theory corrected with the
181 Prandtl tip-loss model are used to predict aerodynamic loads acting on the blades. Meanwhile, the
182 Beddoes-Leishman dynamic stall model is applied for the correction of unsteady aerodynamic
183 performance. In HydroDyn, the wave velocity and acceleration histories are generated using Airy
184 wave theory based on a prescribed wave spectrum. Morison's equations are used to obtain the viscous
185 drag of the support structure. In addition, the hydrostatic restoring contributions of buoyancy and the
186 effect of added mass are taken into account. In the ServoDyn module, the pitch angle of each blade
187 and generator speed are controlled for a stable operation through a dynamic link library or an interface
188 with MATLAB/Simulink. In ElastDyn, the dynamic responses influenced by environment loads are
189 calculated. The wind turbine system is treated as a multi-body system consisting of rigid and flexible
190 bodies. A linear modal approach is applied in structural modelling of flexible bodies (blades and
191 tower). The modal mass participation factor of the consecutive eigenmodes considered for structural
192 modelling should be over 85% [45]. For the wind turbine adopted in this study, the 1^{st} and 2^{nd} flapwise
193 modes and the 1^{st} edgewise mode contribute 87% modal mass of the blade [46]. The neglect of higher
194 modes has a weak influence on the structural responses as confirmed by comprehensive comparisons
195 between FAST and HAWC2 which employs the geometrically exact beam theory for the structural
196 modelling [21, 47-48]. Similarly, the comparison between FAST and ADAMS confirms that the 1^{st}
197 and 2^{nd} fore-aft and side-side modes of tower are efficient enough to represent tower modelling [49-
198 50].

199 The computation of structural responses is done based on the prediction of environmental loads

of the preceding simulation step. Since environmental loads are known to be influenced by the motions of the structures for the next time steps, the structural responses and external loads are fully coupled in the tool. The fourth-order Runge-Kutta method is used for the execution of the time marching simulation.

2.2 Structural modelling of the support structure

The NREL 5 MW wind turbine, developed to support studies that focus on analysis of onshore and offshore wind technology, is used in this study. The rated wind and rotational speeds of the model are 11.4 m/s and 12.1 rpm, respectively. The 1^{st} and 2^{nd} blade collective flap mode frequencies are 0.70 Hz and 2.02 Hz, respectively. The frequency of the 1^{st} edgewise mode is 1.08 Hz. Further details of the wind turbine properties are provided in [46]. The monopile support structure proposed in the phase I of the Offshore Code Comparison Collaboration (OC3) project [21] is applied in this study. As presented in Fig. 2, the monopile has a section of 10 m above the mean sea level (MSL) and a length of 36 m underneath the mudline. The soil condition used in this study is adopted from the OC3 project. A layered soil profile with soil density increasing with depth is selected. The upper soil layer is less dense and stiff while the lower layer is denser and stiffer to ensure a sufficient foundation bearing capacity of the soil. It is assumed that the soil bearing capacities and other properties remain unchanged during the external loadings. The thickness, effective soil weight and angle of internal friction corresponding to each soil layer are presented in Fig .2.

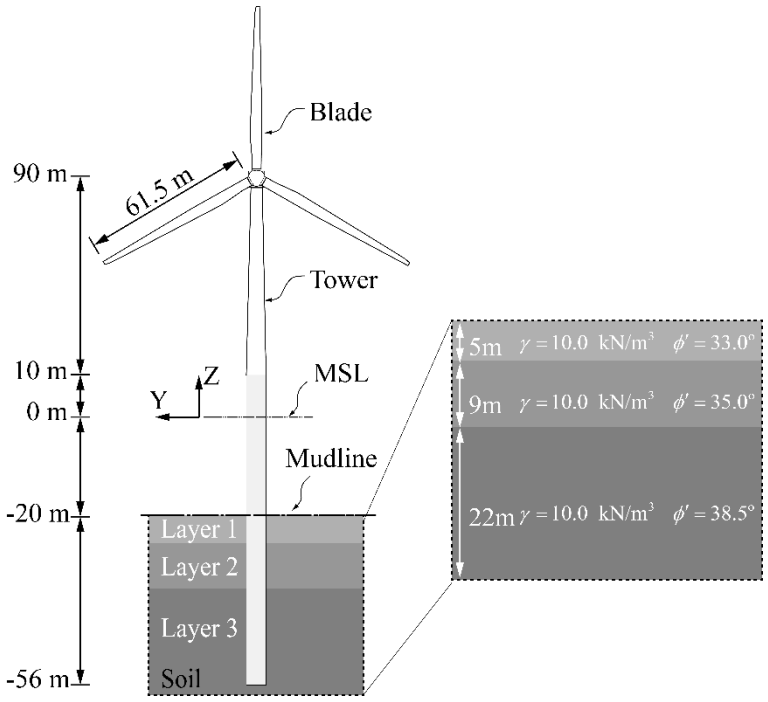

Fig. 2: Schematic diagram of the NREL 5 MW wind turbine geometry

The support structure, which consists of the tower and monopile, is treated as an inverted cantilever beam with a point mass attached to the top. The displacement of the support structure, $u(h,t)$, is represented by the sum of the normal mode shapes of dominant eigenmodes and the associated generalized coordinates [51]:

$$u(h,t)=\sum_{i=1}^{N} q_i(t)\phi_i(h) \tag{1}$$

where $u(h,t)$ represents the displacement at the local height of h and at the time moment of t. $\phi_i(h)$ and $q_i(t)$ are the normal mode shape and the generalized coordinates of the ith eigenmode, respectively. N is the number of the dominant modes and is equal to 4 herein.

According to the Rayleigh-Ritz method, each normal mode shape can be represented by a linear combination of 5 shape functions as follows:

$$\phi_i(h)=\sum_{j=2}^{6} P_{i,j}\varphi_j(h) \quad (i=1,2,3,4) \tag{2}$$

where $P_{i,j}$ is the polynomial coefficient of the jth shape function for the ith normal mode. Before performing a simulation, the five polynomial coefficients of the shape functions for each normal mode

should be given. $\varphi_j(h)$ is the *j*th shape function defined as:

$$\varphi_j(h)=\left(h/H\right)^j \tag{3}$$

where *H* is the total height of the support structure.

The equation of motion for the support structure is derived using Lagrange's equation as follows.

$$\sum_{j=1}^{4} m_{i,j}\cdot\ddot{u}_i(t)+\sum_{j=1}^{4} k_{i,j}\cdot u_i(t)=F_r\ ,\ i=1,2,3,4 \tag{4}$$

where $\ddot{u}_i(t)$ and $u_i(t)$ are respectively the acceleration and velocity corresponding to the *i*th mode. $m_{i,j}$ and $k_{i,j}$ are the generalized mass and stiffness respectively and derived as shown below using the Thomson-Dahleh approach.

$$m_{i,j}=m_{\mathrm{Top}}+\int_0^H \rho(h)\cdot\phi_i(h)\cdot\phi_j(h)\cdot\mathrm{d}h \tag{5}$$

$$k_{i,j}=\int_0^H E(h)\cdot I(h)\cdot\ddot{\phi}_i(h)\cdot\ddot{\phi}_j(h)\cdot\mathrm{dh}-g\int_0^H\left[m_{\mathrm{Top}}+\int_h^H \rho(x)\cdot\mathrm{d}x\right]\cdot\dot{\phi}_i(h)\cdot\dot{\phi}_j(h)\cdot\mathrm{dh} \tag{6}$$

where m_{Top} is the point mass on the top of the support structure. *g* is the gravitational acceleration. $E(h)$ and $I(h)$ are the elastic modulus and the moment of inertia, respectively. $\rho(x)$ is the mass density of the support structure at the local height *x*.

Assuming the support structure vibrates at the *i*th natural mode, the generic solution of the generalized coordinate, $q_i(t)$, can be represented by:

$$q_i(t)=A_i\sin(\omega_i t+\psi_i) \tag{7}$$

where A_i,ω_i and ψ_i are the respective amplitude, natural frequency and phase angle associated with the *i*th eigenmode.

Substituting Eq. (7) and Eq. (1) into Eq. (4), the eigenvalue equation can be written as follows:

$$\left(-\omega^2\boldsymbol{M}+\boldsymbol{K}\right)\boldsymbol{P}=0 \tag{8}$$

where $\boldsymbol{M}$ and $\boldsymbol{K}$ are the respective mass and stiffness matrices while $\boldsymbol{P}$ is the coefficient vector.

The natural frequency and coefficients associated with each mode of the support structure can be

obtained by solving the constitutive equation presented in Eq. (8). Subsequently, the forced vibration equation is defined in terms of the generalized coordinates, $\boldsymbol{q}$, associated with the dominant modes of the support structure:

$$\boldsymbol{M}^* \cdot \ddot{\boldsymbol{q}} + \boldsymbol{C}^* \cdot \dot{\boldsymbol{q}} + \boldsymbol{K}^* \cdot \boldsymbol{q} = \boldsymbol{F}_r^* \tag{9}$$

where $\boldsymbol{M}^*$, $\boldsymbol{C}^*$ and $\boldsymbol{K}^*$ are the respective modal mass, damping and stiffness matrices while $\boldsymbol{F}_r^*$ is the vector of modal forces associated with the dominant modes.

The modal mass and stiffness are defined as:

$$\boldsymbol{M}^* = \sum_{i=1}^{4} \phi_i^{\mathrm{T}} \cdot m \cdot \phi_i \tag{10}$$

$$\boldsymbol{K}^* = \sum_{i=1}^{4} \phi_i^{\mathrm{T}} \cdot k \cdot \phi_i \tag{11}$$

where ϕ_i^{T} is the transposed vector of the i^{th} normalized mode shape ϕ_i of the support structure. m and k are mass and stiffness distributions along the support structure.

The modal damping can be obtained as follows:

$$\boldsymbol{C}^* = 2\xi\sqrt{\boldsymbol{K}^* \cdot \boldsymbol{M}^*} \tag{12}$$

where ξ is the structural damping and a value of 1% is adopted herein [46].

For each mode, the modal force is calculated using:

$$F_i = \int_0^H f(h) \cdot \phi_i(h) \cdot \mathrm{d}h \tag{13}$$

where F_i is the modal force associated with the ith mode. $f(h)$ is the active forces including aerodynamic, hydrodynamic, gravitational and other external forces. Seismic force is also included if the wind turbine is subjected to an earthquake. The Runge-Kutta method is applied for time marching solution of Eq. (9) in order to obtain the displacement, velocity and acceleration of the support structure.

2.3 Flexible foundation models

In order to examine the SSI effect in seismic analysis of a wind turbine, the portion of the support structure underneath the mudline is modelled as a flexible foundation using three distinct methods. A model of the NREL 5 MW wind turbine is presented in Fig. 2 while a schematic diagram of the loading distributions on a wind turbine with different foundations including the rigid type is presented in Fig. 3.

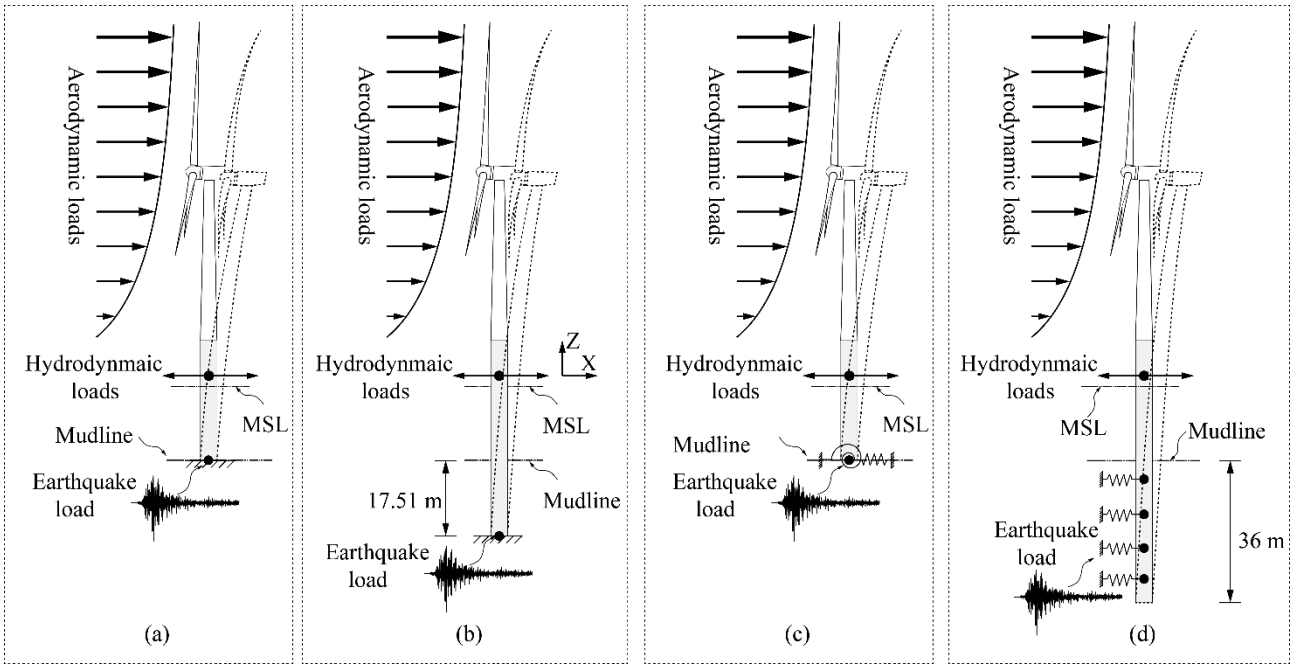

Fig. 3: The loading distributions on a wind turbine modelled with: (a) rigid foundation and different flexible foundations using: (b) AF, (c) CS and (d) DS methods

The basic idea of the AF approach is that a fictive cantilever beam replaces the sub-soil layers of the monopile. Under the combined excitation of a shear force F and a moment M, the fictive equivalent cantilever beam shall produce the same lateral deflection w and rotation θ at the mudline compared to a non-linear SSI model. The w and θ produced by the equivalent cantilever beam with an apparent fixity length of l can be derived as:

$$w=\frac{l^3}{3EI}F+\frac{l^2}{2EI}M \tag{14}$$

$$\theta=\frac{l^2}{2EI}F+\frac{l}{EI}M \tag{15}$$

where EI is the bending stiffness of the fictive structure. l is the fictive length.

According to [52], the w and θ at the mudline under the excitation of 1.24×10^{8} N and 3.91×10^{6} N·m are 2.264×10^{-2} m and 2.413×10^{-3} rad, respectively. The value of the apparent fixity length is obtained as 17.51 m and the diameter and wall thickness of the fictive beam are selected as 6.21 m and 59.9 mm [52]. The material properties are the same as those of the support structure above the mudline.

For the CS approach, the translational and rotational degrees of freedom (DOFs) of the support structure at the mudline are represented by a set of coupled springs. The stiffness of the springs and other directional properties of the remaining DOFs are derived based on pile analysis using LPILE 4.0 [52]. The stiffness matrix $\boldsymbol{K}_{\text{soil,CS}}$ at the mudline is given by:

$$\boldsymbol{K}_{\text{soil,CS}}=\begin{bmatrix} k_{xx} & 0 & 0 & 0 & k_{x\beta} & 0 \\ 0 & k_{yy} & 0 & k_{y\alpha} & 0 & 0 \\ 0 & 0 & 0 & 0 & 0 & 0 \\ 0 & k_{\alpha y} & 0 & k_{\alpha a} & 0 & 0 \\ k_{\beta x} & 0 & 0 & 0 & k_{\beta\beta} & 0 \\ 0 & 0 & 0 & 0 & 0 & 0 \end{bmatrix} \tag{16}$$

where x and y are the translational directions in the horizontal plane, α and β represent the rotational directions about the corresponding axis, respectively. The values of the stiffness are presented in Table 1.

The load vector, $\boldsymbol{F}_{\text{soil}}$, acting at the bottom of the support structure produced by the soil flexibility can be derived as:

$$\boldsymbol{F}_{\text{soil}} = \boldsymbol{K}_{\text{soil,CS}} \bullet \boldsymbol{U} + \boldsymbol{C}_{\text{soil,CS}} \bullet \dot{\boldsymbol{U}} \tag{17}$$

where $\boldsymbol{K}_{\text{soil,CS}}$ is the stiffness matrix as denoted in Eq. (16). $\boldsymbol{C}_{\text{soil,CS}}$ is the damping matrix. The transitional damping effects are ignored since the rotational damping effects are dominant [53]. The rotational damping values are 9.34×10^{8} Nms/rad. $\boldsymbol{U}$ and $\dot{\boldsymbol{U}}$ are the respective displacement and velocity vectors of the support structure at the mudline.

Table 1: Stiffness properties of the CS model

Item	Value	Item	Value
k_{xx}	2.57481×10^{9} N/m	k_{yy}	2.57481×10^{9} N/m
$k_{x\beta}$	-2.25325×10^{10} N/rad	$k_{\beta x}$	-2.25325×10^{10} Nm/m
$k_{y\alpha}$	2.25325×10^{10} N/rad	$k_{\alpha y}$	2.25325×10^{10} Nm/m
$k_{\alpha a}$	2.62912×10^{11} Nm/rad	$k_{\beta\beta}$	2.62912×10^{11} Nm/rad

In the DS model, the SSI effect is represented by a set of linear lateral springs distributed along the pile length beneath the mudline. The stiffness of each spring is derived by using a *p-y* curve. The modelling of the soil condition is the same as in the AF model and the stiffness distribution along the pile is presented in Fig. 4. The values of the stiffness distribution have been validated through comprehensive comparisons between different numerical results [21, 48].

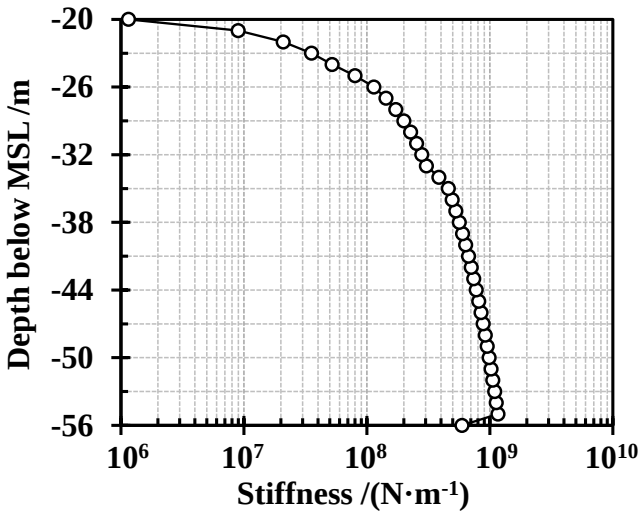

Fig. 4: Stiffness distribution of the springs along the pile and underneath the mudline [52]

The horizontal force acting on the pile underneath the seabed and produced by the soil flexibility by ignoring the damping effects is denoted as:

$$\begin{cases} F_{\mathrm{X,Z}} = K_{\mathrm{Z}} \cdot U_{\mathrm{X,Z}} \\ F_{\mathrm{Y,Z}} = K_{\mathrm{Z}} \cdot U_{\mathrm{Y,Z}} \end{cases} \tag{18}$$

where X, Y and Z represent the longitudinal, lateral and vertical directions as defined in Fig. 2 and Fig. 3. K_Z is the stiffness at the depth of Z referred to Fig. 4. $U_{X,Z}$ and $U_{Y,Z}$ are the horizontal displacements of the pile at the depth of Z.

In Table 2, the natural frequencies of the first two eigenmodes of the support structure in fore-aft and side-side directions are presented for comparisons with the results from reference [52]. The flexible foundation models have a smaller natural frequency for each eigenmode compared to the fixed-base model. The results agree well with the reference regarding the first modes in the fore-aft and side-side directions, especially in the AF and DS models. The AF and DS models have a deviation of 11% for the 2nd fore-aft eigenmode compared to the results of the reference due to the act that the tower top mass moment of inertia is not considered in the reference, while their frequencies of the 2nd side-side mode are similar. These comparisons validate the flexible foundations modelled in this study by confirming that it could well represent the actual foundation model of a wind turbine. The normalized modal shapes of the four models above the mudline (Fig. 5) did not show any significant discrepancy between the modal shapes of the AF and DS models. This suggests that the difference between the dynamic responses of the two models above seabed might be insignificant.

Table 2: Natural frequencies of the support structure (unit: Hz)

	Fixed-base	AF model	CS model	DS model	Ref. [52]
1st fore-aft	0.276	0.246	0.247	0.247	0.248
1st side-side	0.274	0.245	0.246	0.245	0.246
2nd fore-aft	1.867	1.51	1.732	1.512	1.546
2nd side-side	1.589	1.359	1.497	1.358	1.533

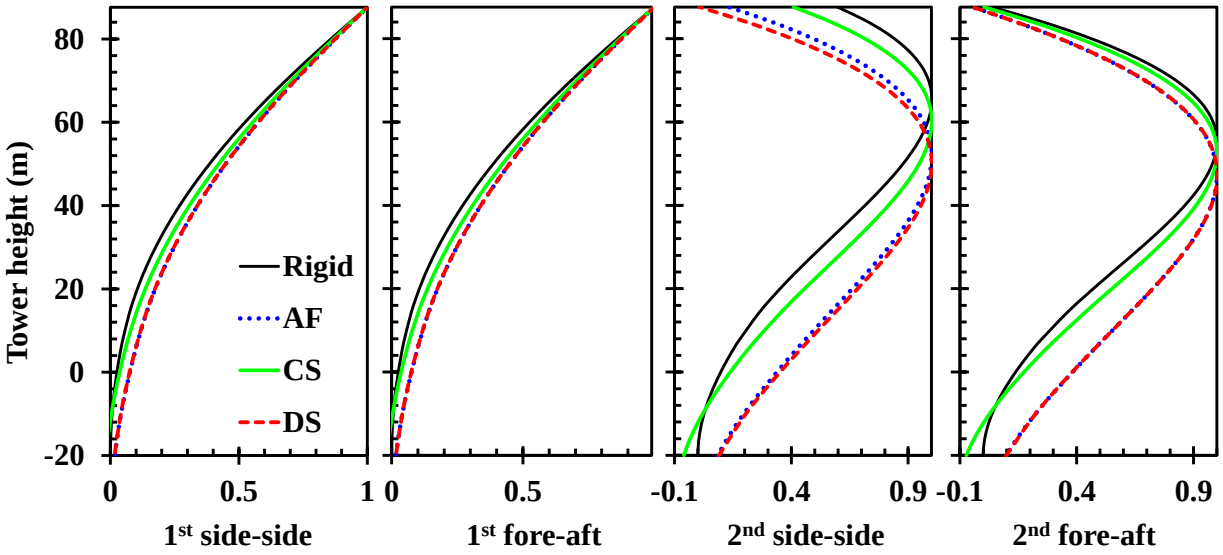

Fig. 5: Normalized modal shapes corresponded to the models

2.4 Development of the seismic module (SAF)

In order to perform the analysis of offshore wind turbines influenced by multiple loadings including wind, wave and earthquake, a seismic module written in FORTRAN has been integrated into the baseline FAST to develop SAF as presented in Fig. 6.

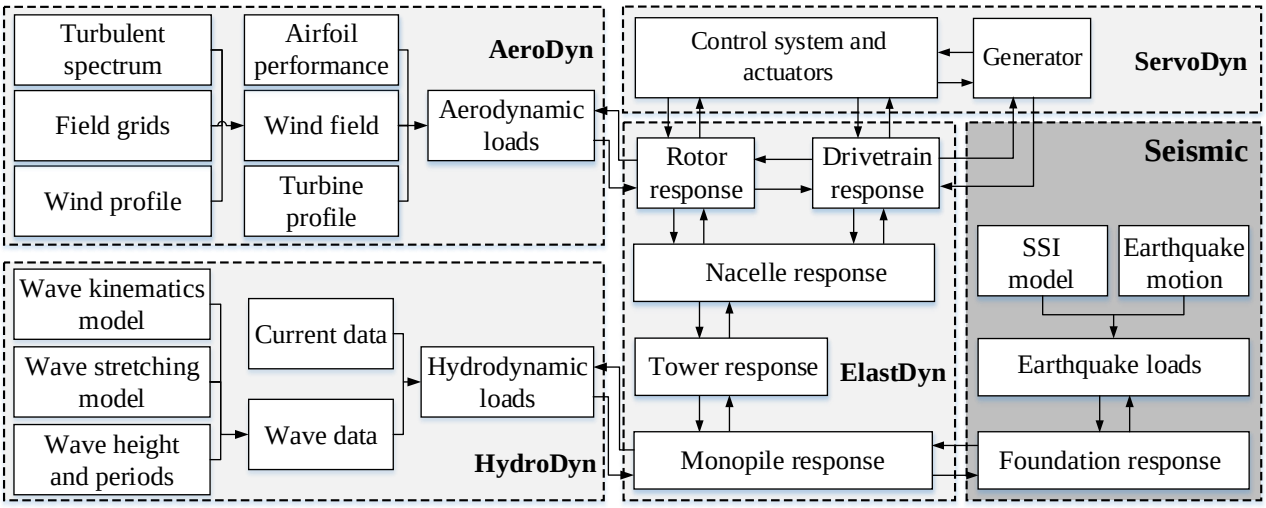

Fig. 6: Schematic diagram of SAF for offshore wind turbines

In the seismic module, a specified earthquake motion is required for the computation of seismic force. Baseline correction is applied to the input motion in order to eliminate a large drift of ground

displacement caused by potential numerical errors and measurement noises [14]. The earthquake force acting on the support structure is added to the modal forces within FAST. For each mode considered in this study, the corresponding earthquake force, $F_{\mathrm{eq},i}$, is calculated by:

$$F_{\mathrm{eq},i} = a_{\mathrm{eq}} \cdot \int_0^H [m(h) \cdot \phi_i(h)]\mathrm{d}h \qquad i = 1,2,3,4 \tag{19}$$

where $F_{\mathrm{eq},i}$ represents the earthquake force associated with the *i*th eigenmode. $m(h)$ is the mass distribution density along the support structure. a_{eq} is the specified earthquake acceleration.

The earthquake force obtained in the seismic module is included in the modal forces as expressed in Eq. (9) and it is coupled with other environment loads to obtain the structural responses. The method of earthquake force calculation used in this study is consistent with that employed for seismic analysis of buildings. One of the benefits of using SAF is that it is generic and can be applied to different types of wind turbine models compared with the NREL Seismic tool.

3 Loading conditions

3.1 Full-field turbulent wind

TurbSim [54] developed by NREL is used to generate the full-field turbulent wind for simulations. The wind field centred on hub is discretized in finite grids in both the horizontal and vertical directions. The size of the wind field adopted to cover the operating domain of the wind turbine in this study is 175 m × 200 m (Fig. 7). The velocity component in *x* direction is perpendicular to the rotor plane while the directions of the other two components are also depicted in Fig. 7.

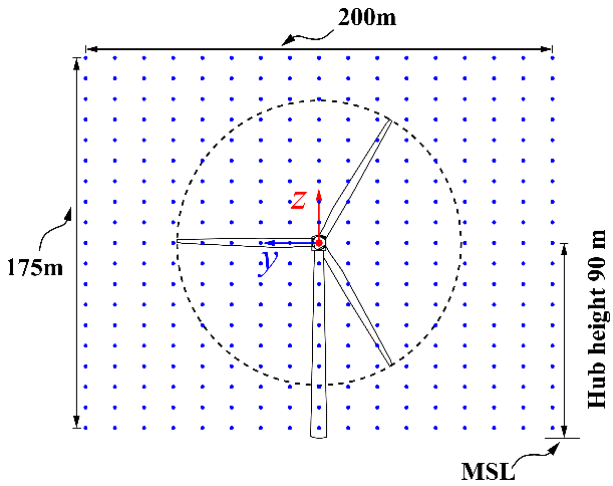

Fig. 7: Grid discretization of wind filed domain

Time-varying wind speed of each grid can be represented by the sum of a constant component $\bar{V}$ and a turbulent component $\tilde{V}(t)$. The constant component at a height of h is calculated using the power law profile with an exponent of 0.2 as follows:

$$\bar{V}(h) = V_{\text{hub}} \left(h / H_{\text{hub}} \right)^{0.2} \tag{20}$$

where V_{hub} is the mean velocity at the hub height of H_{hub}. The value of V_{hub} is selected as 11.4 m/s equal to the rated wind speed.

The turbulent component $\tilde{V}(t)$ is calculated by applying an Inverse Fast Fourier Transformation (IFFT) to the IEC Kaimal turbulent spectrum described by:

$$S_\gamma(f) = \frac{4\sigma_\gamma^2 L_\gamma V^{-1}}{(1+6fL_\gamma V^{-1})^{5/3}} \quad \gamma = x, y, z \tag{21}$$

where f is the frequency, V is the mean wind speed at the hub height, σ_γ is the standard deviation of the wind speed and L_γ is the integral scale parameter of each velocity component.

The turbulence intensity is selected as level A (19.86% at hub). In accordance with IEC-64000-1, the standard deviations of the wind speed are 2.2 m/s, 1.76 m/s and 1.1 m/s for x, y and z directions, respectively. The values of L_γ are 486 m, 162 m and 39.6 m for x, y and z directions, respectively.

In order to include the spatial dependency of wind speed at different grids, the cross spectra between two grids i and j are expressed as:

$$S_{i,j}(f) = C(\Delta r, f)\sqrt{S_{i,i}(f) \cdot S_{j,j}(f)} \tag{22}$$

where $S_{i,j}(f)$ is the cross spectrum, $S_{i,i}(f)$ and $S_{j,j}(f)$ are the spectra at grids i and j, respectively. $C(\Delta r, f)$ is the coherence function between grids i and j as given in Eq. (23) in reference to IEC-640001-1.

$$C(\Delta r, f) = \exp\left[-a\sqrt{\left(\frac{f\Delta r}{V_{\text{hub}}}\right)^2 + \left(\frac{0.12\Delta r}{L_c}\right)^2}\right] \tag{23}$$

where Δr is the distance between the two grids. a is the coherence decrement with a value of 12 adopted in this study. L_c is the coherence scale parameter with a value of 340.2 m.

The generated wind field is presented in Fig. 8. The time-varying wind speed at hub has a peak value of over 20 m/s and an average magnitude of 11.4 m/s as expected. The variation of wind speed at each grid is irregular in time domain and non-uniform in spatial distribution indicating that the generated wind field has turbulent characteristics.

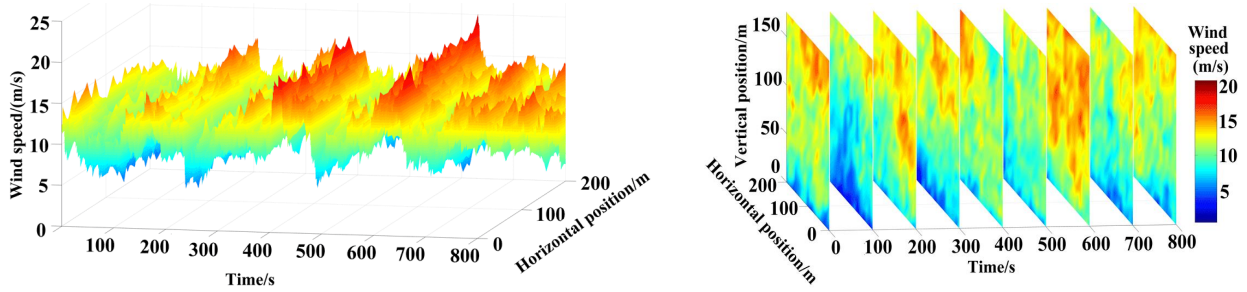

Fig. 8: The full-field turbulent wind: (a) time-varying wind speed at hub height and (b) wind speed distribution of rotor plane at different time steps

3.2 Irregular wave and current

The hydrodynamic loads acting on the support structure are determined using Morison's equation [55]. The hydrodynamic force $F(t)$ acting on the moving support structure can be written as:

$$F(t)=\int_0^H C_M\rho\frac{1}{4}\pi D^2\dot{V}(z,t)\mathrm{d}z-(C_M-1)\rho\frac{1}{4}\pi D^2\dot{U}(z,t)\mathrm{d}z \\ +\frac{1}{2}C_D\rho D\left[V(z,t)-U(z,t)\right]\left|V(z,t)-U(z,t)\right|\mathrm{d}z \tag{24}$$

where H is the height of the support structure. C_M and C_D are the normalized hydrodynamic added mass and viscous drag coefficients. The values adopted herein are 1.6 and 1.0, respectively. ρ is the density of sea water; D is the diameter of the support structure, $V(z,t)$ and $U(z,t)$ are the wave velocity and structure moving velocity, respectively. $\dot{V}(z,t)$ and $\dot{U}(z,t)$ are the wave and structure moving accelerations, respectively.

The JONSWAP spectrum [56] as denoted in Eq. (25) is used to generate the wave time histories.

$$S_\zeta(\omega)=0.3125H_s^2T_p\left(\frac{\omega}{\omega_p}\right)^5\exp\left[-\frac{5}{4}\left(\frac{\omega}{\omega_p}\right)^{-4}\right](1-0.287\ln\chi)\chi^{\exp\left[-\frac{(\omega-\omega_p)^2}{2\sigma^2\omega_p^2}\right]}} \tag{25}$$

where H_s is the significant wave height and T_p is the wave period. The adopted values of H_s and T_p are 6 m and 9.9 s, respectively. $\omega_p=2\pi/T_p$, $\sigma=0.07$ for $\omega\le\omega_p$ and $\sigma=0.09$ for $\omega>\omega_p$. χ represents the JONSWAP peakedness parameter selected in terms of:

$$\chi=\begin{cases}5 & T_p/\sqrt{H_s}\le 3.6\\ \exp(5.75-1.15T_p/\sqrt{H_s}) & 3.6<T_p/\sqrt{H_s}\le 5\\ 1 & T_p/\sqrt{H_s}>5\end{cases} \tag{26}$$

According to Airy theory [57], the wave time histories can be written as:

$$\eta(t)=\sum_{j=1}^{N}A_j\sin(w_j\cdot t-k_j\cdot\chi+\psi_j) \tag{27}$$

$$A_j=\sqrt{2S_\zeta(\omega_j)\Delta\omega} \tag{28}$$

$$V(z,t)=\sum_{j=1}^{N}\omega_jA_j\frac{\cosh\left[k(z+d_w)\right]}{T_p\sinh(kd_w)}\sin(\omega_jt-k_j\cdot\chi+\psi_j) \tag{29}$$

$$\dot{V}(z,t)=\sum_{j=1}^{N}\omega_j^2A_j\frac{\cosh\left[k(z+d_w)\right]}{T_p\sinh(kd_w)}\cos(\omega_j\cdot t-k_j\cdot\chi+\psi_j) \tag{30}$$

where $\eta(t)$ is the wave elevation time history. ω is the wave frequency in rad/s. ψ_j is a random phase angle falling within 0 to 2π . d_w is the water depth, *i.e.* the distance between the mudline and MSL. *z* is the local water depth. *k* is the wave number related with *z* and ω as expressed in Eq. (31).

$$k\tanh(kz) = \omega^2/g \tag{31}$$

where *g* is the gravitational acceleration.

For a specified water depth *z*, the wave number can be obtained by solving Eq. (31) to calculate the wave time histories.

The current velocity at the local water depth z is calculated using a power law [58].

$$V_c(z) = V_0(\frac{z+h}{h})^{1/7} \tag{32}$$

where V_0 is the current velocity at MSL. The adopted value in this research is 0.55 m/s.

3.3 Earthquake motions

In order to achieve the set out goals of this study, a set of 28 earthquake records are selected from the PEER NGA database [59] using the criteria suggested in [60]. In detail, the magnitudes of the earthquake records fall within the range of M6.5 to M8.0. The PGA for each record is larger than 0.2 g or the peak of the ground velocity (PGV) is larger than 15 cm/s. Based on the selection criteria, 28 earthquake records are selected from 14 events that occurred between 1976 and 2002. Each of these records contains two horizontal components and the average magnitude of the records is M7.0. Most of the selected earthquake events occurred near coastline, *e.g.* California in the USA and Kocaeli in Turkey. A summary of the selected records is presented in Appendix A.

Since the selected ground motions were recorded at different sites, it means that the frequency contents of the ground motions might be inconsistent with the geological characteristics of the selected site for the offshore wind turbine. The frequency contents of the time-varying accelerations

of the ground motions have been modified using the target response spectrum matching technique in order to be consistent with the location of the measured earthquake. The 28 earthquake records selected in this study are therefore adjusted to match the corresponding response spectra which are specified in accordance with the American Society of Civil Engineers (ASCE) 7-10 standard [61].

As presented in the ASCE 7-10 standard, each of the target response spectra is given by specifying the design spectral accelerations within the 'short periods' and the period of 1.0 second as presented in Fig. 9 [60].

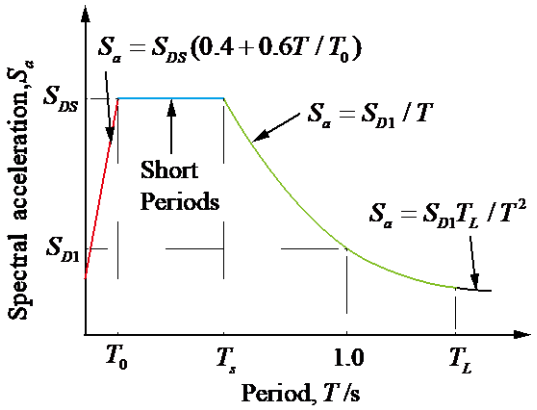

Fig. 9: A target response spectrum defined in ASCE 7-10 standard

In Fig.9, S_{DS} and S_{D1} are the design spectral response acceleration within 'short periods' and at the period of 1.0 second, respectively, T_L is the long-period transition period which is usually larger than 10 seconds, T_0 and T_s are the starting and ending values of the 'short periods' calculated as below:

$$T_0 = 0.2S_{D1} / S_{DS} \tag{33}$$

$$T_S = S_{D1} / S_{DS} \tag{34}$$

In accordance with the site classification presented in the ASCE 7-10 standard, the soil condition applied in this study is classified as Class D. For each of the two horizontal components of a selected earthquake record, the value of S_{DS} is adopted as 2.5 times of the PGA and the value of S_{D1} equals

466 the PGA. The "RspMatch" code developed by Atik et al [62] is used to adjust the frequency contents
467 of the ground motions and the detailed matching procedure can be found in [63]. In order to illustrate
468 the spectral matching effect, Fig.10 presents the initial and adjusted spectral accelerations
469 corresponding to the Imperial Valley earthquake record (ID No. 1 in Appendix A). It is anticipated
470 that the discrepancies between the initial and target response spectra in both directions have been
471 effectively eliminated. This indicates that the adjusted ground motion can efficiently represent the
472 frequency characteristics of the earthquake in the specific site. It is apparent that the intensity of the
473 adjusted ground motion is larger than the initial one since significant increases of the spectral
474 accelerations in both directions are observed within the 'short periods'. The time history accelerations
475 of the initial and adjusted ground motions are presented in Fig.11. The PGAs of the initial ground
476 motion in the *x* and *y* directions were 0.353 g and 0.337 g, respectively. The PGAs corresponding to
477 the adjusted ground motion are 0.432 g and 0.549 g, respectively. It confirms that the adjusted ground
478 motion has the requisite intensity defined by the target spectrum.

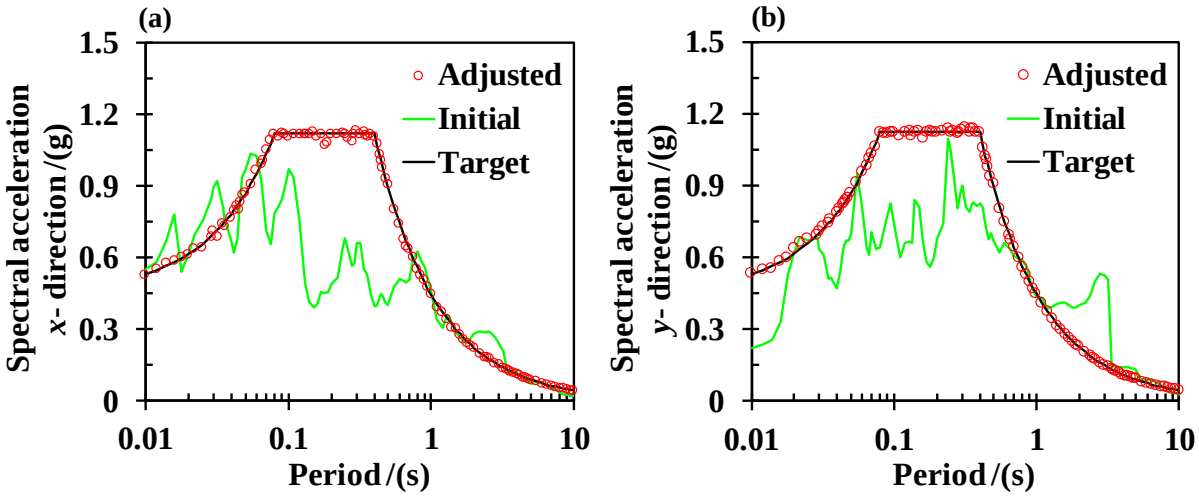

479

480 Fig. 10: The initial, target and adjusted response spectral accelerations at (a) *x* direction and (b) *y*
481 direction

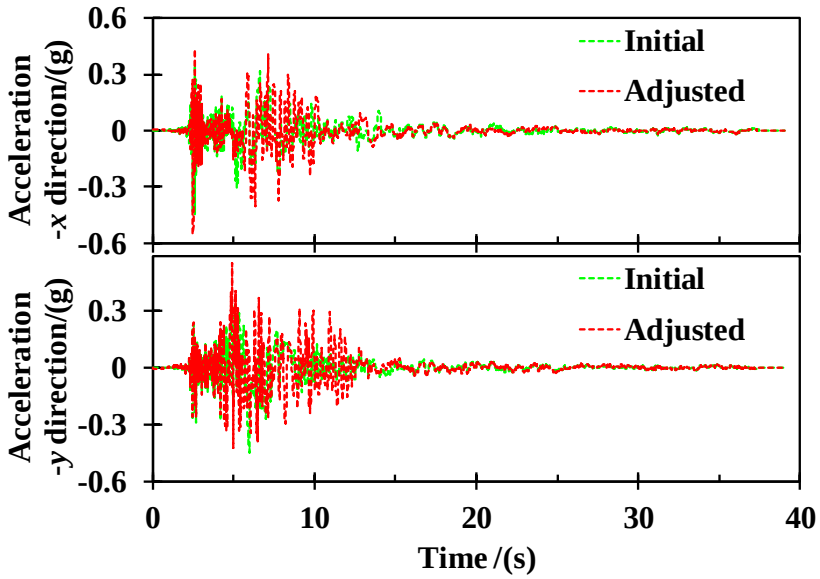

Fig. 11: Time history accelerations of the initial and adjusted ground motions

The root mean square (RMS) adjusted spectra of the earthquake records with a damping of 5% are presented in Fig. 12. The pseudo spectral acceleration (PSA) is the spectral acceleration of an earthquake record corresponding to a fundamental period. The PSA is a characteristic parameter that reflects the influence of the earthquake on the structure. As can be seen, the fundamental period of the 2nd eigenmode of each model falls within the range of significant PSA. It means that the activation of the 2nd mode may have a notable contribution to the seismic dynamic response of the wind turbine.

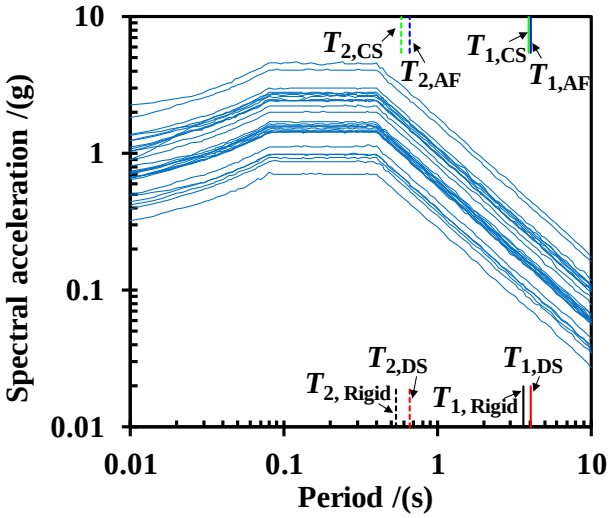

Fig. 12: Spectral accelerations of earthquake records

Acceleration time histories of the earthquake records are also available in the PEER NGA database. Seismic loads are calculated using SAF based on the acceleration data obtained from [59].

4 Results and discussions

4.1 Validation for the developed SAF

In order to validate the computational accuracy of SAF, dynamic responses of the NREL 5 MW monopile wind turbine predicted using SAF and GH Bladed are compared. In addition, a comparison between SAF and the NREL Seismic tool is also presented. The choice of these tools (GH Bladed and NREL Seismic) was driven by the fact that they were thoroughly validated using experimental results, hence their wide acceptance in the industry. The ground accelerations of Northridge earthquake event which occurred in 1994 are selected as the input motion. The earthquake starts at the 400^{th} s for a 600 s simulation to ensure that the transient response induced by wind is diminished.

The time-varying mudline bending moments of the support structure predicted using all the different numerical tools used in this study are presented in Fig. 13. The variations of mudline moments predicted using SAF agree well with the results obtained using GH Bladed and NREL Seismic during the strong shaking period of the earthquake event (405 s ~ 425 s). The maximum mudline moments computed using SAF, GH Bladed and NREL Seismic are 129 MN·m, 133 MN·m and 138 MN·m, respectively. The deviation of the maximum mudline moment between the results obtained using SAF and GH Bladed is 3%, while the corresponding deviation received using SAF and NREL Seismic is 6%. The two sets of the results are within the industry tolerance of 10%. The comparisons confirmed that SAF has a good reliability for the prediction of seismic dynamic responses.

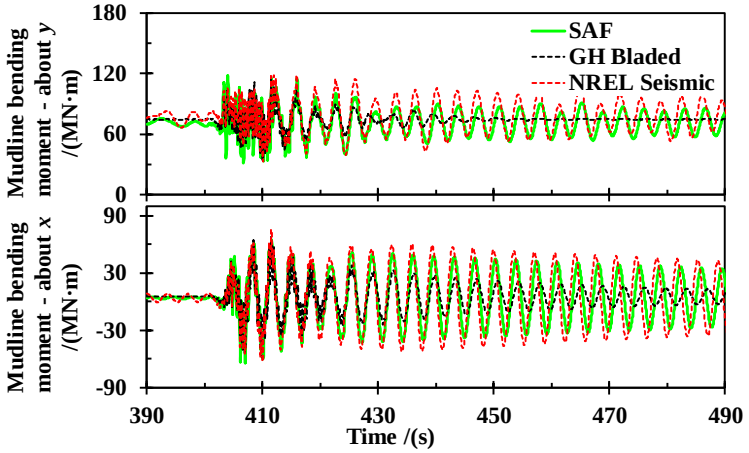

Fig. 13: Comparisons of time domain results calculated using the reference tools and SAF

The frequency domain responses are obtained by applying the Fast Fourier Transformation (FFT) to the time domain results, as presented in Fig. 14. For the bending moment about *y*-axis (out-of-plane), the amplitudes at the 1st and 2nd natural frequencies of the results from SAF agree well with those predicted using GH Bladed and NREL Seismic. Regarding the bending moment about *x*-axis (in-plane), the amplitude at the 1st eigenmode frequency is equal to the results from GH Bladed and NREL Seismic, but the amplitude of the 2nd natural frequency is slightly smaller than the ones predicted using the reference tools. The comparisons for the frequency domain results further indicate that SAF can be used to accurately predict the seismic responses of offshore wind turbines. It is expected that following the validation and demonstration of this approach, SAF is expected to be used by designers looking for a generic and cost-effective tool for the design of wind turbine foundations in earthquake prone areas.

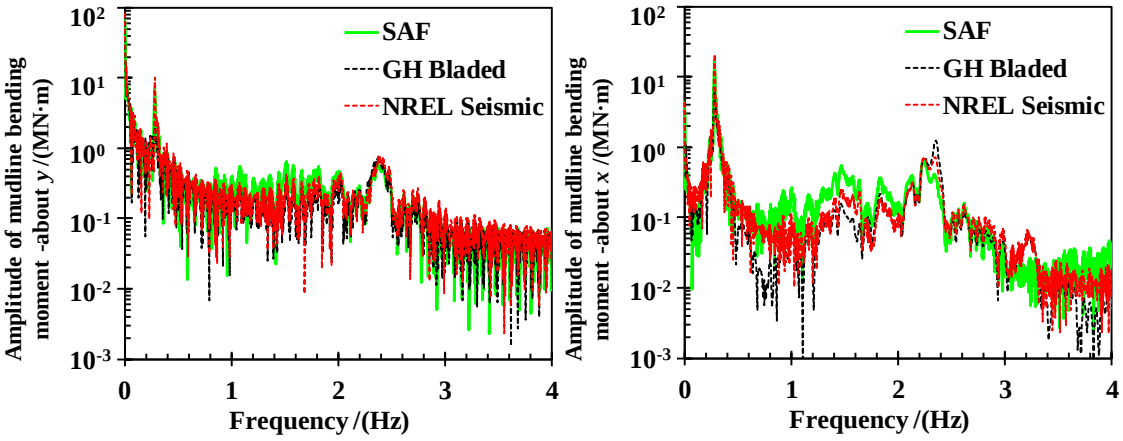

527 Fig.14: Comparisons of the frequency domain results calculated using reference tools and SAF

528

529 ## *4.2 Responses to an earthquake event*

530 In order to obtain a preliminary insight into the sensitivity of the flexible foundation models,
531 dynamic responses of the offshore wind turbine subjected to a single earthquake event are obtained.
532 The Imperial Valley earthquake record with a PGA of 0.448 g (ID No. 1 in Appendix A) is selected
533 as the input ground motion. The average wind speed at the hub of the wind field is 11.4 m/s. The
534 significant height of the irregular wave is 6 m and the wave period is 9.9 s. The JONSWAP spectrum
535 is used to generate the wave histories according to the methods presented in section 3.2. The current
536 velocity at MSL is adopted as 0.55 m/s. The earthquake is assumed to occur at 400^{th} s in a 600 s
537 simulation with a time step of 0.002 s.

538 Tower-top displacements of the wind turbine with different foundation models under the
539 earthquake excitation are presented in Fig. 15. The displacements increase significantly with values
540 fluctuating once the earthquake occurs (> 400 s). A notable difference can be observed from the results
541 of rigid and flexible foundation models. The peaks of the displacements in both directions of the rigid
542 foundation model are smaller than those of the flexible foundation models. This can be explained by
543 considering that the vibration induced by the earthquake is more severe in flexible foundations
544 compared to a rigid foundation. The flexible foundation models have lower eigen-frequencies, which
545 means the eigenmodes are more easily excited due to smaller energy level demand. Regarding the
546 fore-aft displacement, although the contribution of elastic deformation produced by the aerodynamic
547 load is dominant, the contribution of vibration amplitude is significant during the strong shaking
548 period (405 s ~ 415 s). As a result, the fore-aft displacement of the flexible models is larger than that
549 of the rigid model.

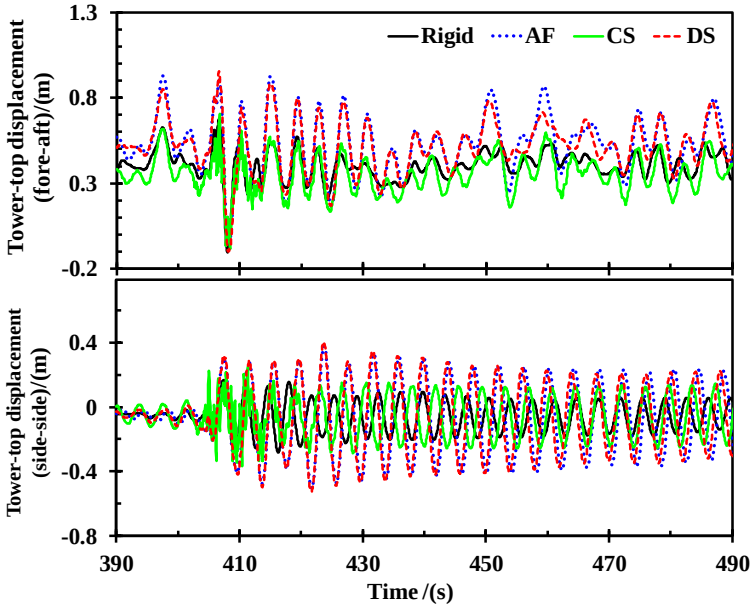

Fig. 15: Tower-top displacements of the wind turbine with different foundation models

It can be further observed that the AF and DS models have similar responses but with a slight difference in the variation period as expected due to similar modal frequencies. The responses from the AF and DS models are larger than those from the CS model.

With the application of FFT, the amplitudes of tower-top displacements in frequency domain are obtained and presented in Fig. 16. It is noted that the 1st eigenmodes in both fore-aft (FA) and side-side (SS) directions are activated for all the examined models, while the activation of the 2nd mode in each direction is only visible in the CS model. The amplitudes at the 1st natural frequency of flexible foundation models are larger than those of the rigid foundation model in both directions. Once again, this indicates that the amplitude of vibration induced by the earthquake excitation for the flexible foundation models is larger compared to the rigid foundation model. In both fore-aft and side-side directions, the amplitudes of the 1st natural frequency of AF and DS models are of similar sizes and they are larger than those of the CS model, while the rigid foundation model has the smallest amplitude at the corresponding 1st natural frequency.

The comparisons indicate that the soil effect has a notable influence on seismic responses of the wind turbine. This implies that the flexibility of foundation must be taken into account when

567 performing seismic analysis.

568

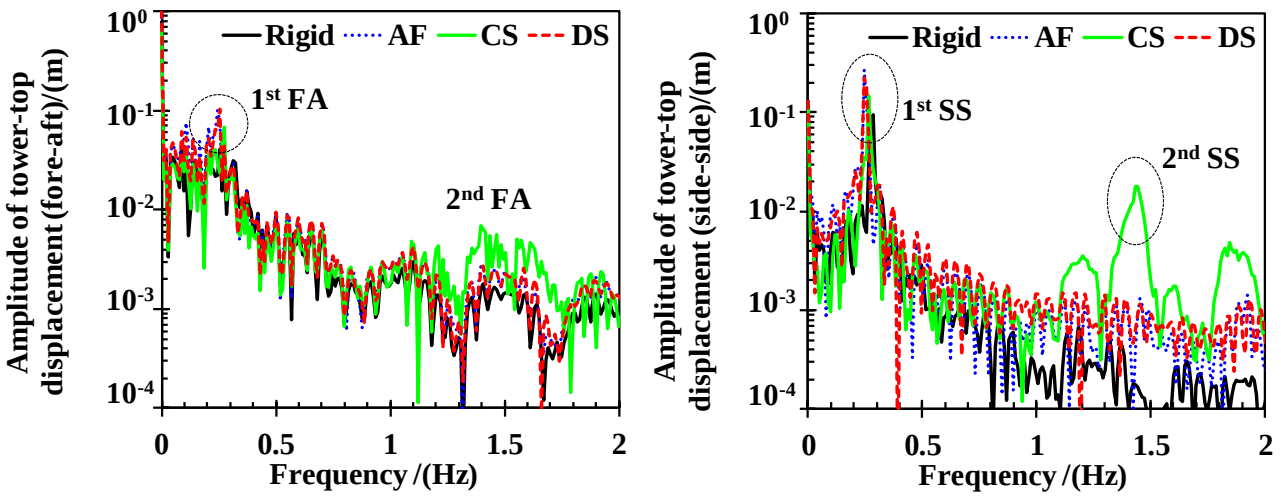

569

570 Fig. 16: Amplitude of tower-top displacements in frequency domain

571

572 Time-varying bending moments of the support structure at the mudline and the corresponding
573 frequency domain results are presented in Fig. 17 and Fig. 18, respectively. It is notable that the
574 mudline bending moment of the rigid foundation model is larger than those for the flexible foundation
575 models. Regarding the in-plane mudline bending moment, a significant discrepancy is observed in
576 the magnitudes of the different foundation models. The maximum magnitude of the rigid model is
577 214 MN·m, while the corresponding values for the AF, CS and DS models are 119 MN·m, 94 MN·m
578 and 148 MN·m, respectively.

579 Although the 2nd eigenmode of the support structure and the 2nd flapwise mode of the blade have
580 been activated for the flexible foundation models, peaks at the 2nd modal frequencies are one order
581 lower than those at the 1st fore-aft mode frequency, implying that the main contribution to the in-
582 plane bending moment comes from the 1st mode with exception of the rigid model. In addition, in
583 terms of the out-of-plane bending moment at the mudline, the amplitudes at 0 Hz of the rigid, AF, CS
584 and DS models are 117.9 MN·m, 120.3 MN·m, 119.2 MN·m and 119.9 MN·m respectively. It is

noted that the amplitudes are much higher than the peak values at the 1st side-side mode frequencies and this is attributed to the effect of wind loading. It can be stated that the wind loading has a dominant impact on the out-of-plane bending moment for the examined wind and earthquake conditions. This can further explain why the difference among the out-of-plane bending moments of the foundation models is insignificant.

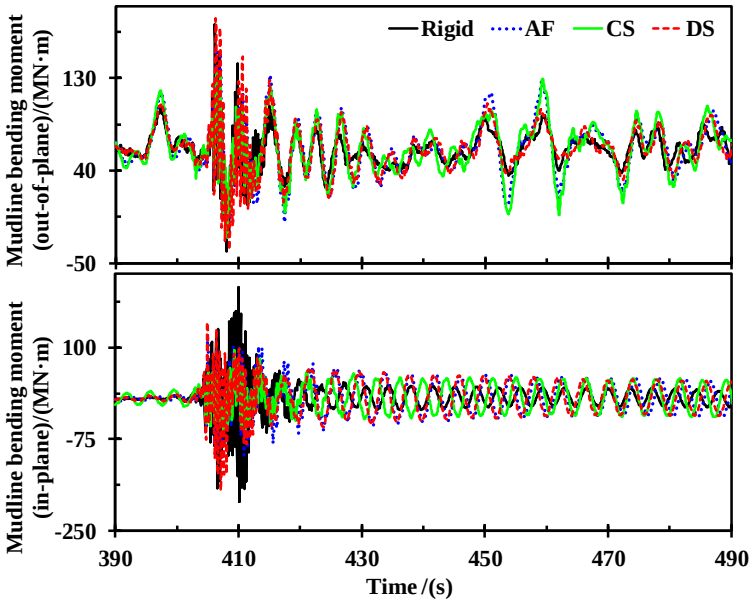

Fig. 17: Time-varying bending moments of the support structure at the mudline

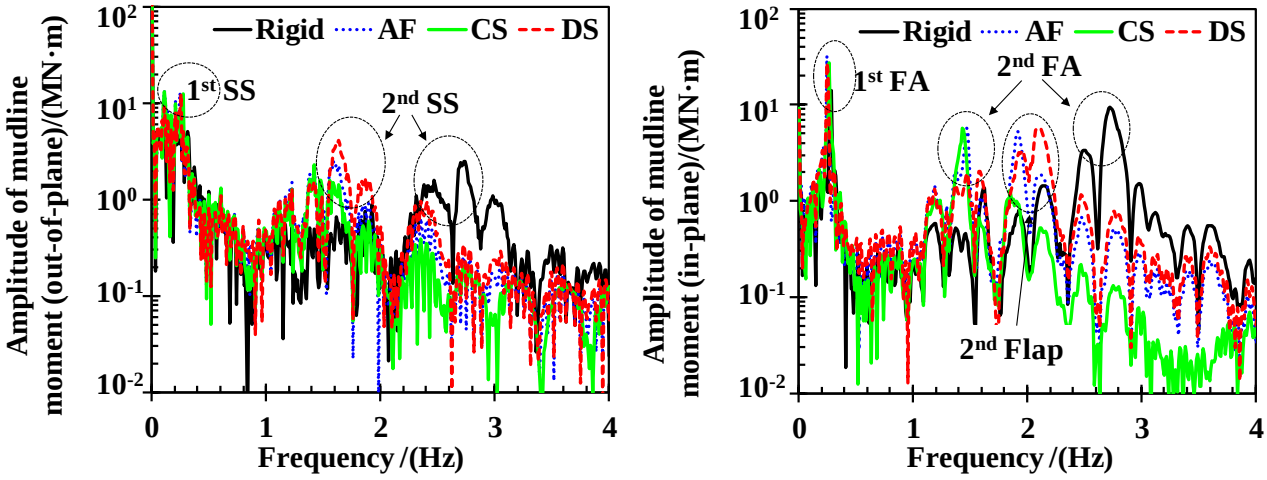

Fig. 18: Frequency domain results of mudline bending moments

The peak distributions of displacement and acceleration along the support structure and above

597 the mudline are presented in Fig.19. The displacement profiles show that the combined loadings
598 activate the 1st eigenmode of the support structure. The AF model has the highest tower-top
599 displacement, while the corresponding value of the rigid model is the smallest. Compared to the DS
600 model, the rigid, the CS and AF models underestimate the displacements, while the AF model has the
601 smallest deviation, implying that the AF model has a relative higher accuracy for the response
602 calculation.

603 The activation of the 2nd mode of the support structures is visible for all the examined models as
604 confirmed by the acceleration profiles. As can be seen, significant values are observed from the
605 acceleration distributions at approximately 60 m above the MSL that is consistent with the 2nd modal
606 shape profiles as shown in Fig. 5. In addition, the rigid model overestimates the acceleration at a
607 tower height above 30 m and underestimates the results at a tower height of less than 30 m compared
608 to the DS model. The prediction for the CS model is conservative for heights above 5 m. The
609 difference between the results of the AF and DS models is relatively small. It can be argued that the
610 SSI effect is better addressed with the use of the AF model than the CS model.

611

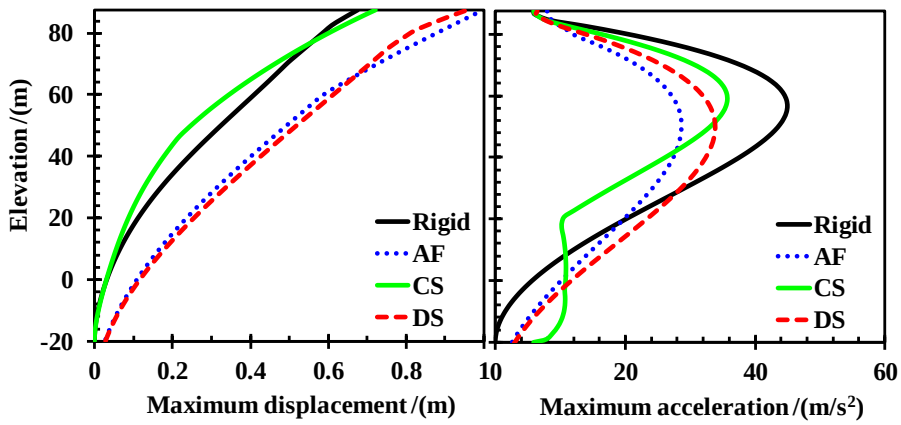

612

613 Fig. 19: Peak distributions of displacement and acceleration along the support structure

614

615 Fig. 20 presents the distributions of maximum loads acting on the support structure. The

maximum bending moments decrease along with the support structure height, this result is consistent with the analogous results of the same wind turbine calculated using the boundary element method [10]. The maximum bending moment of the rigid model at the mudline is close to that of the DS model, while a significant difference is observed for the AF and CS models. In terms of the maximum shear force, the prediction for the CS model is the largest at the mudline. The deviation between the CS model and DS model is larger than that between the AF and DS models. The results from this investigation imply that the AF model can predict responses more accurately compared to the CS model.

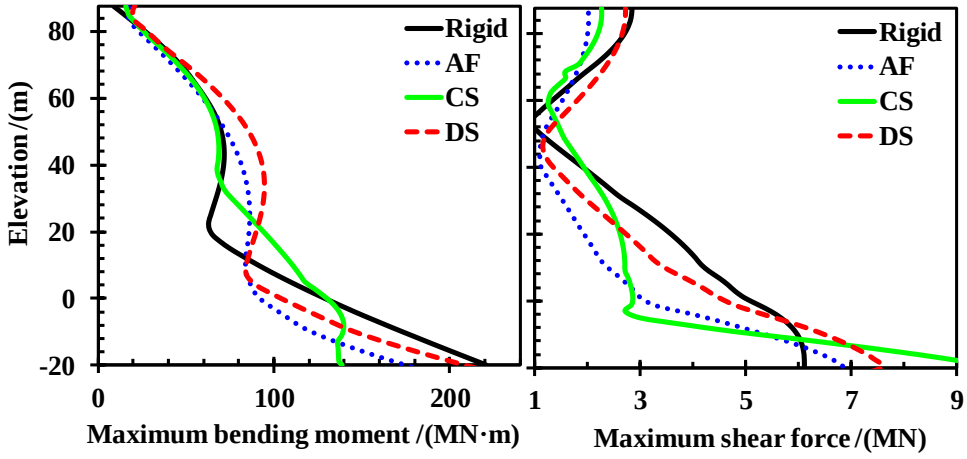

Fig. 20: Peak distributions of the bending moment and shear force along the support structure

4.3 Trends of maximum responses related with PSA

A set of earthquake data is selected as input ground motions in order to investigate the seismic behaviour of wind turbines influenced by different earthquake intensities. For each of the 28 earthquake records listed in Appendix A, two simulations are conducted for each foundation model, which interchanges the horizontal components to reduce the biases due to relative orientation with the wind direction. The peak values of the responses from the two simulations for each earthquake

event are averaged. In total, 224 simulations have been conducted for the rigid model and the three flexible foundation models.

The average peaks of the tower-top displacement for the four foundation models versus PSA at the 1st fundamental period are presented in Fig. 21. The dash lines represent the response level without earthquake excitations. The black, blue, green and red lines represent the result from rigid, AF, CS and DS models, respectively. As can be observed, the AF model has excitation values that are similar to those of the DS model but they are larger when compared to the CS and rigid models. The peak tower-top displacement increases with PSA almost linearly for all the examined models when the PSA is larger than 0.1 g, while the influence of PSA is insignificant when the PSA is lower than 0.1g. This is because the wind loading dominates the tower-top displacement if the underlying loading comes from an earthquake with a low intensity excitation. In this condition, the elastic deformation is the main contributor to the displacement rather than the vibration amplitude dominated by the earthquake loading. In addition, the main contribution to the vibration amplitude at tower-top comes from the 1st eigenmode as stated and illustrated previously. This further affirms why the peak tower-top displacement is sensitive to PSA at the 1st fundamental period.

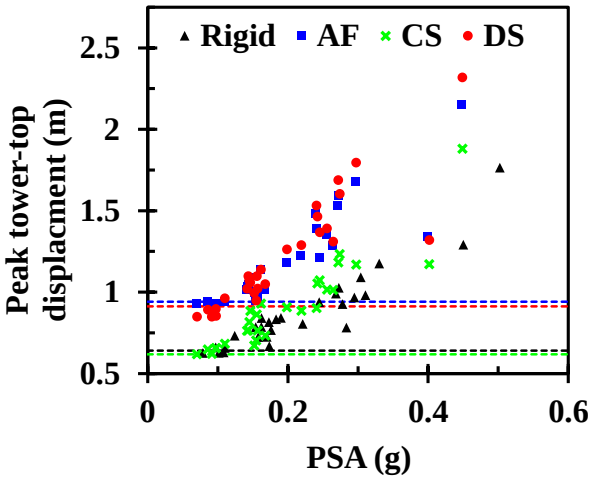

Fig. 21: The peak tower-top displacement versus PSA

The maximum bending moments at the mudline for the examined models versus PSA are

presented in Fig. 22. For each record, the DS model has a larger mudline bending moment compared to the AF and CS models, indicating that the AF and CS models would potentially underestimate the bending moment at the mudline. Similar to the observations from the tower-top displacement, the mudline moment approximately increases linearly with the PSA. It should be noted that the predictions of the rigid model are higher compared to the flexible models. This confirms that ignoring the soil effect will overestimate the bending moments of the wind turbine.

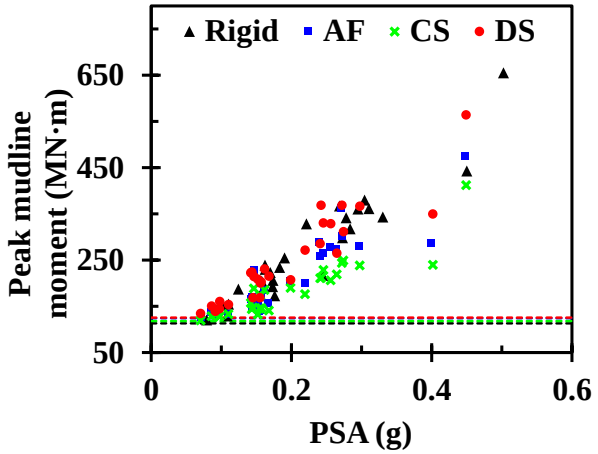

Fig. 22: The peak mudline bending moment versus PSA

Fig. 23 presents the peak bending moment at blade-root versus PSA for the examined models. As can be observed, the response level of the CS and rigid models is closer to the level without earthquake loading for most of the examined cases. In this condition, it was anticipated that the blade dynamic response is dominated by wind loading which turned out to be correct. While earthquake loading has a significant influence on the blade bending moments for the AF and DS models, it can be explained by considering that the eigenmode of the blade has been activated by earthquakes as shown in Fig. 18. It is further observed that the increasing trend of the blade-root moment is nearly linear with the PSA for the AF and DS model, while the linear trend is not obvious for the rigid and CS models. Similarly, the rigid, AF and CS models underestimate the blade-root bending moment compared to the DS model. The AF model has a relatively smaller difference when compared to the

670 CS model.

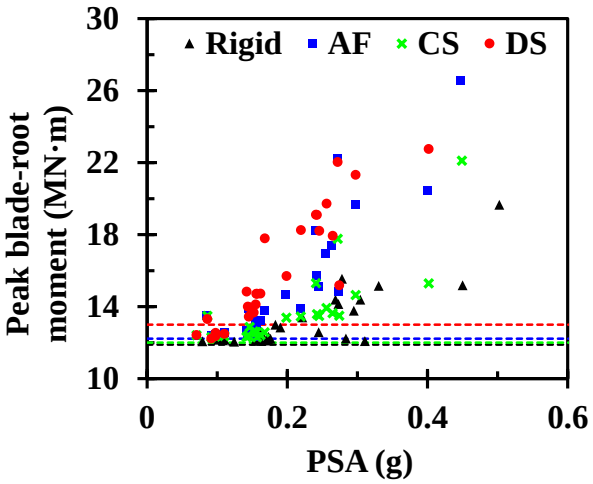

671

672 Fig. 23: The peak blade-root bending moment versus PSA

673 ## 5 Conclusions

674 In this study, the sensitivity of foundation models to the dynamic behaviour of an offshore wind
675 turbine under earthquake loadings has been investigated. In order to consider the influence of flexible
676 foundation and earthquake loading, SAF is developed and implemented in an open source tool named
677 FAST. The validation of SAF is carried out through comparisons with some experimentally validated
678 numerical tools, GH Bladed and NREL Seismic. Three distinct flexible foundation models are
679 established for the NREL 5 MW offshore wind turbine using the AF, CS and DS methods. An
680 earthquake dataset of 28 records is selected as input ground motions. The earthquake records are
681 scaled using the target spectrum matching technique defined in accordance with the ASCE 7-10
682 standard. In total, 224 fully coupled nonlinear simulations have been conducted. Based on the results
683 and discussions described, the following four key conclusions are given:

684 (1) A generic SAF is developed and presented to investigate the sensitivity of the foundation
685 model to the dynamic behaviour of an offshore wind turbine subjected to multiple loadings
686 including wind and earthquake. Comparisons against alternative numerical tools are
687 presented. Good agreements between the results in both time and frequency domains are

observed, indicating that SAF has a high accuracy and reliability to conduct seismic behaviour assessment for offshore wind turbines.

(2) The AF and DS models have larger displacement at tower-top in fore-aft and side-side directions due to more severe vibrations induced by earthquakes. The tower-top vibration amplitudes of the flexible models are larger compared to the rigid model as observed in the spectra. The 1st eigenmodes in both fore-aft and side-side directions dominate the vibration, meanwhile the activations of the 2nd eigenmodes are visible in the examined cases.

(3) The main contribution to the out-of-plane bending moment at the mudline for all foundation models could come from wind loading as observed from the frequency domain results associated with specific loading of the examined conditions. In terms of the mudline bending moment, the influence of the 1st eigenmode is more significant than that of the 2nd eigenmode. Activation of the 2nd flap mode of blade is observed from the spectra of in-plane bending moments for the AF and DS models, while it is invisible in the rigid and CS models.

(4) The peak tower-top displacement increases linearly with PSA for all the foundation models while the trend is also visible for mudline bending moments. Due to the contribution of the blade eigenmode, the blade-root bending moment of the AF and DS models is more sensitive to earthquake loading compared to the CS and rigid models. Moreover, it is noted that the results from the AF model are closer to the ones from the DS model in terms of the magnitudes and trends. Therefore, the AF model can be used to produce realistic results compared to the CS model.

Acknowledgements

The authors would like to acknowledge the financial supports from the National Natural Science Foundation of China (grant numbers: 51676131 and 51811530315) and Royal Society (grant number:

711 IEC\NSFC\170054). This project is partially supported by the European Union's Horizon 2020
712 Research and Innovation Programme, RISE, under grant agreement no. 730888 (RESET) and
713 European Regional Development Fund (ERDF), Interreg Atlantic Area (grant number:
714 EAPA_344/2016). The first author (Yang Yang) and the last author (Chunmin Yang) are particularly
715 grateful to the Chinese Scholarship Council for funding their overseas studies in the UK.

716

Appendix A. Summary of earthquake records

The summary of earthquake records applied in this study for seismic analysis is listed below.

ID No.	Earthquake Name	Year	Station	Magnitude	PGA (g)	PGA/(g) (Scaled)
1	Imperial Valley-06	1979	El Centro Array #6	6.53	0.448	0.589
2	Imperial Valley-06	1979	El Centro Array #7	6.53	0.437	0.623
3	Imperial Valley-06	1979	Bonds Corner	6.53	0.687	0.399
4	Imperial Valley-06	1979	Chihuahua	6.53	0.265	0.597
5	Superstition Hills-02	1987	Parachute Test Site	6.54	0.433	0.671
6	Erzican, Turkey	1992	Erzincan	6.69	0.445	0.626
7	Northridge-01	1994	Rinaldi Receiving Sta	6.69	0.708	0.910
8	Northridge-01	1994	Sylmar - Olive View Med FF	6.69	0.640	1.009
9	Northridge-01	1994	LA - Sepulveda VA Hospital	6.69	0.753	1.084
10	Northridge-01	1994	Northridge - 17645 Saticoy St	6.69	0.388	1.096
11	Nahanni, Canada	1985	Site 1	6.76	1.160	0.306
12	Nahanni, Canada	1985	Site 2	6.76	0.398	0.965
13	Gazli, USSR	1976	Karakyr	6.80	0.702	0.319
14	Irpinia, Italy-01	1980	Sturno (STN)	6.90	0.282	0.654
15	Loma Prieta	1989	Saratoga - Aloha Ave	6.93	0.369	2.123
16	Loma Prieta	1989	BRAN	6.93	0.463	0.983
17	Loma Prieta	1989	Corralitos	6.93	0.500	0.323
18	Cape Mendocino	1992	Petrolia	7.01	0.624	2.650
19	Cape Mendocino	1992	Cape Mendocino	7.01	1.396	0.728
20	Duzce, Turkey	1999	Duzce	7.14	0.434	0.650
21	Landers	1992	Lucerne	7.28	0.727	0.903
22	Kocaeli, Turkey	1999	Izmit	7.51	0.194	2.086
23	Kocaeli, Turkey	1999	Yarimca	7.51	0.286	1.113
24	Chi-Chi, Taiwan	1999	TCU065	7.62	0.689	0.588
25	Chi-Chi, Taiwan	1999	TCU102	7.62	0.267	0.466
26	Chi-Chi, Taiwan	1999	TCU067	7.62	0.425	0.621
27	Chi-Chi, Taiwan	1999	TCU084	7.62	0.738	1.306
28	Denali, Alaska	2002	TAPS Pump Station #10	7.90	0.324	0.400

References

[1] GWEC, Global Wind Energy Council. "Global Wind Report: Annual Market Update 2017."*http://gwec.net/cost-competitiveness-puts-wind-in-front/.*[Accessed May 18, 2018] (2018).

[2] Bazeos, N., Hatzigeorgiou, G. D., Hondros, I. D., Karamaneas, H., Karabalis, D. L. & Beskos, D. E. (2002). Static, seismic and stability analyses of a prototype wind turbine steel tower. *Engineering Structures*, 24(8), 1015-1025.

[3] Lavassas, I., Nikolaidis, G., Zervas, P., Efthimiou, E., Doudoumis, I. N. & Baniotopoulos, C. C. (2003). Analysis and design of the prototype of a steel 1-MW wind turbine tower. *Engineering Structures*, 25(8), 1097-1106.

[4] Hacıefendioğlu, K. (2012). Stochastic seismic response analysis of offshore wind turbine including fluid‐structure‐soil interaction. *The Structural Design of Tall and Special Buildings*, 21(12), 867-878.

[5] Ma, H. & Zhang, D. (2016). Seismic response of a prestressed concrete wind turbine tower. *International Journal of Civil Engineering*, 14(8), 561-571.

[6] Patil, A., Jung, S. & Kwon, O. S. (2016). Structural performance of a parked wind turbine tower subjected to strong ground motions. *Engineering Structures*, 120, 92-102.

[7] Smith, V. & Mahmoud, H. (2016). Multihazard assessment of wind turbine towers under simultaneous application of wind, operation, and seismic loads. *Journal of Performance of Constructed Facilities*, 30(6), 04016043.

[8] Zhao, X. & Maisser, P. (2006). Seismic response analysis of wind turbine towers including soil-structure interaction. *Proceedings of the Institution of Mechanical Engineers, Part K: Journal of Multi-body Dynamics*, 220(1), 53-61.

[9] Sapountzakis, E. J., Dikaros, I. C., Kampitsis, A. E. & Koroneou, A. D. (2015). Nonlinear response of wind turbines under wind and seismic excitations with soil–structure interaction. *Journal of Computational and Nonlinear Dynamics*, 10(4), 041007.

[10] Yang, Y., Ye, K., Li, C., Michailides, C. & Zhang, W. (2018). Dynamic behavior of wind turbines influenced by aerodynamic damping and earthquake intensity. *Wind Energy*, 21 (5), 303-319.

[11] Witcher, D. (2005). Seismic analysis of wind turbines in the time domain. *Wind Energy*, 8(1), 81-91.

750 [12] Santangelo, F., Failla, G., Santini, A. & Arena, F. (2016). Time-domain uncoupled analyses for
751 seismic assessment of land-based wind turbines. *Engineering Structures*, 123, 275-299.
752 [13] Asareh, M. A., Prowell, I., Volz, J. & Schonberg, W. (2016). A computational platform for
753 considering the effects of aerodynamic and seismic load combination for utility scale horizontal
754 axis wind turbines. *Earthquake Engineering and Engineering Vibration*, 15(1), 91-102.
755 [14] Asareh, M. A. & Prowell, I. (2011). Seismic loading for FAST. *(No. NREL/SR-5000-53872),*
756 *National Renewable Energy Laboratory*, Golden, CO.
757 [15] Asareh, M. A., Schonberg, W. & Volz, J. (2016). Effects of seismic and aerodynamic load
758 interaction on structural dynamic response of multi-megawatt utility scale horizontal axis wind
759 turbines. *Renewable energy*, 86, 49-58.
760 [16] Jin, X., Liu, H. & Ju, W. (2014). Wind Turbine Seismic Load Analysis Based on Numerical
761 Calculation. *Strojniski Vestnik/Journal of Mechanical Engineering*, 60(10).
762 [17] Katsanos, E. I., Sanz, A. A., Georgakis, C. T. & Thöns, S. (2017). Multi-hazard response analysis
763 of a 5 MW offshore wind turbine. *Procedia Engineering*, 199, 3206-3211.
764 [18] Randolph, M., Gourvenec, S., White, D. & Cassidy, M. (2011). Offshore geotechnical
765 engineering (Vol. 2). New York: Spon Press.
766 [19] Wang, X., Yang, X. & Zeng, X. (2017). Seismic centrifuge modelling of suction bucket
767 foundation for offshore wind turbine. Renewable energy, 114, 1013-1022.
768 [20] Bhattacharya, S. (2014). Challenges in design of foundations for offshore wind turbines.
769 Engineering & Technology Reference, 1(1), 922.
770 [21] Jonkman, J. & Musial, W. (2010). Offshore code comparison collaboration (OC3) for IEA Wind
771 Task 23 offshore wind technology and deployment. *(No. NREL/TP-5000-48191). National*
772 *Renewable Energy Laboratory.(NREL)*, Golden, CO (United States).
773 [22] Harte, M., Basu, B. & Nielsen, S. R. (2012). Dynamic analysis of wind turbines including soil-
774 structure interaction. Engineering Structures, 45, 509-518.
775 [23] Carswell, W., Johansson, J., Løvholt, F., Arwade, S. R., Madshus, C., DeGroot, D. J. & Myers,
776 A. T. (2015). Foundation damping and the dynamics of offshore wind turbine monopiles.
777 Renewable energy, 80, 724-736.
778 [24] Damgaard, M., Andersen, L. V. & Ibsen, L. B. (2015). Dynamic response sensitivity of an
779 offshore wind turbine for varying subsoil conditions. Ocean engineering, 101, 227-234.
780 [25] Arany, L., Bhattacharya, S., Macdonald, J. H. & Hogan, S. J. (2016). Closed form solution of

781 Eigen frequency of monopile supported offshore wind turbines in deeper waters incorporating
782 stiffness of substructure and SSI. Soil Dynamics and Earthquake Engineering, 83, 18-32.
783 [26] Sun, C. (2018). Mitigation of offshore wind turbine responses under wind and wave loading:
784 Considering soil effects and damage. Structural Control and Health Monitoring, 25(3), e2117.
785 [27] Failla, G., Santangelo, F., Foti, G., Scali, F. & Arena, F. (2018). Response-Spectrum Uncoupled
786 Analyses for Seismic Assessment of Offshore Wind Turbines. Journal of Marine Science and
787 Engineering, 6(3), 85.
788 [28] Bhattacharya, S. & Adhikari, S. (2011). Experimental validation of soil–structure interaction of
789 offshore wind turbines. Soil Dynamics and Earthquake Engineering, 31(5-6), 805-816.
790 [29] Lombardi, D., Bhattacharya, S. & Wood, D. M. (2013). Dynamic soil–structure interaction of
791 monopile supported wind turbines in cohesive soil. Soil Dynamics and Earthquake Engineering,
792 49, 165-180.
793 [30] Bhattacharya, S., Cox, J. & Lombardi, D. (2013). Dynamics of offshore wind turbines on two
794 types of foundations. Proceedings of the Institution of Civil Engineers: Geotechnical Engineering.
795 [31] Damgaard, M., Bayat, M., Andersen, L. V. & Ibsen, L. B. (2014). Assessment of the dynamic
796 behaviour of saturated soil subjected to cyclic loading from offshore monopile wind turbine
797 foundations. Computers and Geotechnics, 61, 116-126.
798 [32] Bisoi, S. & Haldar, S. (2014). Dynamic analysis of offshore wind turbine in clay considering
799 soil–monopile–tower interaction. Soil Dynamics and Earthquake Engineering, 63, 19-35.
800 [33] Prendergast, L. J., Gavin, K. & Doherty, P. (2015). An investigation into the effect of scour on
801 the natural frequency of an offshore wind turbine. Ocean Engineering, 101, 1-11.
802 [34] Bisoi, S. & Haldar, S. (2015). Design of monopile supported offshore wind turbine in clay
803 considering dynamic soil–structure-interaction. Soil Dynamics and Earthquake Engineering, 73,
804 103-117.
805 [35] Shi, W., Park, H. C., Chung, C. W., Shin, H. K., Kim, S. H., Lee, S. S. & Kim, C. W. (2015).
806 Soil-structure interaction on the response of jacket-type offshore wind turbine. International
807 Journal of Precision Engineering and Manufacturing-Green Technology, 2(2), 139-148.
808 [36] Carswell, W., Arwade, S. R., DeGroot, D. J. & Lackner, M. A. (2015). Soil–structure reliability
809 of offshore wind turbine monopile foundations. Wind energy, 18(3), 483-498.
810 [37] Damgaard, M., Zania, V., Andersen, L. V. & Ibsen, L. B. (2014). Effects of soil–structure
811 interaction on real time dynamic response of offshore wind turbines on monopiles. Engineering

812 Structures, 75, 388-401.
813 [38] Santangelo, F., Failla, G., Arena, F. & Ruzzo, C. (2018). On time-domain uncoupled analyses for
814 offshore wind turbines under seismic loads. *Bulletin of Earthquake Engineering*, 16(2), 1007-
815 1040.
816 [39] Kim, D. H., Lee, S. G. & Lee, I. K. (2014). Seismic fragility analysis of 5 MW offshore wind
817 turbine. *Renewable Energy*, 65, 250-256.
818 [40] Mo, R., Kang, H., Li, M. & Zhao, X. (2017). Seismic fragility analysis of monopile offshore
819 wind turbines under different operational conditions. *Energies*, 10(7), 1037.
820 [41] Alati, N., Failla, G. & Arena, F. (2015). Seismic analysis of offshore wind turbines on bottom-
821 fixed support structures. *Philosophical Transactions of the Royal Society A*, 373 (2035),
822 20140086.
823 [42] Sun, C. (2018). Semi-active control of monopile offshore wind turbines under multi-hazards.
824 *Mechanical Systems and Signal Processing*, 99, 285-305.
825 [43] Sun, C. & Jahangiri, V. (2018). Bi-directional vibration control of offshore wind turbines using a
826 3D pendulum tuned mass damper. *Mechanical Systems and Signal Processing*, 105, 338-360.
827 [44] Jonkman, J. M. & Buhl Jr, M. L. (2005). Fast user's guide-updated august 2005 (No. NREL/TP-
828 500-38230). National Renewable Energy Lab.(NREL), Golden, CO (United States).
829 [45] Prowell, I. & Veers, P. (2009). Assessment of wind turbine seismic risk: Existing literature and
830 simple study of tower moment demand. Sandia report, 3.
831 [46] Jonkman, J., Butterfield, S., Musial, W. & Scott, G. (2009). Definition of a 5-MW reference wind
832 turbine for offshore system development. *(No. NREL/TP-500-38060). National Renewable*
833 *Energy Laboratory.(NREL)*, Golden, CO (United States).
834 [47] Buhl, M. & Manjock, A. (2006, January). A comparison of wind turbine aeroelastic codes used
835 for certification. In 44th AIAA Aerospace Sciences Meeting and Exhibit (p. 786).
836 [48] Passon, P., Kühn, M., Butterfield, S., Jonkman, J., Camp, T. & Larsen, T. J. (2007). OC3—
837 benchmark exercise of aero-elastic offshore wind turbine codes. In Journal of Physics:
838 Conference Series (Vol. 75, No. 1, p. 012071). IOP Publishing.
839 [49] Jonkman, J. M. (2007). Dynamics modeling and loads analysis of an offshore floating wind
840 turbine (Vol. 68, No. 11).
841 [50] Cordle, A. & Jonkman, J. (2011). State of the art in floating wind turbine design tools. In The
842 Twenty-first International Offshore and Polar Engineering Conference. International Society of

Offshore and Polar Engineers.

[51] Jonkman, J. M. (2003). Modeling of the UAE wind turbine for refinement of FAST {_} AD. *(No. NREL/TP-500-34755). National Renewable Energy Laboratory*. Golden, CO (US).

[52] Passon, P. (2006). Memorandum: derivation and description of the soil-pile-interaction models. IEA-Annex XXIIII Subtask, 2.

[53] Aasen, S. (2016). Soil-structure interaction modelling for an offshore wind turbine with monopile foundation. *Master's thesis, Norwegian University of Life Sciences*, Oslo.

[54] Jonkman, B. J. (2009). TurbSim user's guide: Version 1.50. *(No. NREL/TP-500-46198). National Renewable Energy Laboratory.(NREL)*, Golden, CO (United States).

[55] Sarpkaya, T. (1986). Force on a circular cylinder in viscous oscillatory flow at low Keulegan—Carpenter numbers. Journal of Fluid Mechanics, 165, 61-71.

[56] Aranuvachapun, S. (1987). Parameters of Jonswap spectral model for surface gravity waves—II. Predictability from real data. Ocean engineering, 14(2), 101-115.

[57] Craik, A. D. (2004). The origins of water wave theory. Annu. Rev. Fluid Mech., 36, 1-28.

[58] Jonkman, J. M., Robertson, A. & Hayman, G. J. (2014). HydroDyn user's guide and theory manual. National Renewable Energy Laboratory.

[59] Pacific Earthquake Engineering Research (PEER) ground motion database. *URL: https://ngawest2.berkeley.edu/*

[60] ATC. (2009). Quantification of building seismic performance factors. Report no. FEMA-P695, *Applied Technology Council*, Redwood City, CA, USA,.

[61] American Society of Civil Engineers & Structural Engineering Institute. Minimum Design Loads on Buildings and Other Structures Standards Committee. (2013). Minimum design loads for buildings and other structures. American Society of Civil Engineers.

[62] Al Atik, L. & Abrahamson, N. (2010). An improved method for nonstationary spectral matching. Earthquake Spectra, 26(3), 601-617.

[63] Hancock, J., Watson-Lamprey, J., Abrahamson, N. A., Bommer, J. J., Markatis, A., McCOY, E. M. M. A. & Mendis, R. (2006). An improved method of matching response spectra of recorded earthquake ground motion using wavelets. Journal of earthquake engineering, 10(spec01), 67-89.